

Aerodynamic Analysis of Wind Turbines Rotors with High Lift Airfoils by Using Pre-conditioned WENO Scheme

J. C. Huang¹, H. Lin², T. Y. Hsieh², J. Y. Yang³
Corresponding author: jchuang@ntou.edu.tw

¹Department of Merchant Marine, National Taiwan Ocean University

²Chung-Shan Institute of Science & Technology,

³Institute of Applied Mechanics, National Taiwan University

Abstract: The aerodynamic analysis of wind turbine rotors using preconditioned weighted essentially non-oscillatory scheme to solve the compressible Navier-Stokes equations in non-inertial coordinate system with Spalart-Allmaras one equation turbulence model is presented. A parallel clustering algorithm based on Message Passing Interface library was implemented. The NREL Phase VI rotor with S809 airfoil was considered as testing configuration and the wind tunnel data from NASA Ames were used to verify the validity and accuracy of present method. The grid refinement test was performed firstly on surface pressure, normal and tangent forces of blade sections and rotor shaft torque. Besides the S809 airfoil, rotors with high lift airfoils DAE21 and FX63100 are also studied to investigate their effects on aerodynamic performance of wind turbine rotors.

Keywords: wind turbine aerodynamics, rotor, blade, airfoil, preconditioned WENO scheme.

1 Introduction

To design a high-efficiency wind turbine rotor, the accurate numerical prediction for the rotor aerodynamic performances can serve as a quicker and lower-cost alternative as compared to wind tunnel experiments. Past studies applied CFD for wind turbine analysis have provided essential information in the design process of turbine rotor. Due to the three-dimensional nature of the low Mach number flow phenomena, most numerical schemes developed for compressible Navier-Stokes equations are often inefficient or even inaccurate since the convective terms of the time dependent system of equations become stiff. In our previous works [1-3], an implicit preconditioned WENO (P-WENO) scheme for steady viscous flow computation was presented. With the P-WENO scheme, the stiffness problem and slow convergence can be overcome and meanwhile high-accuracy for all speeds of flow can be maintained. The P-WENO scheme was used to simulate flows of the NREL Phase VI Rotor using a parallel strategy by adopting a block-domain decomposition method for the patched multi-block grid system.

The configuration of a no twist rotor blade is similar to the high aspect wing of low-speed long endurance aircraft. However, the aircraft wing provides lift force, but the blade provides rotation torque. For aircraft design, the most important subject is to improve the lift-drag ratio, the design of the wing section is very important. The low-Reynolds number high-lift airfoils are widely used in gliders and unmanned aircraft, typical operating Reynolds number of the range about 2×10^5 to 1×10^6 . The issues of flow field simulation of high-lift wing section profile are turbulence model for the separation flow modeling applicability and laminar-turbulent transition [4]. In recent years,

consideration researches studied these issues. For examples, Wolfe and Ochs [5] used the results of experimental data to setting the transition locations at 46% and 40% chord length for the upper and lower surface of S809 airfoil, respectively, and then significantly improve the computational accuracy of S809 airfoil lift and drag coefficient. Xu and Sankar, [6], as well as Benjanirat and Sankar, [7] solved hybrid Navier-Stokes and potential equation with Spalart-Allmaras single equation turbulence model and Eppler boundary layer transfer model [8] to simulating NREL the Phase III and VI rotor flows and obtained good results.

In present work, the P-WENO scheme was used to solve the pre-conditioned Navier-Stokes equations with Spalart-Allmaras single-equation turbulence model, and Eppler, Chen-Thysson transition position computing model [8] in non-inertial frame to simulate the flow field of NREL Phase VI rotor with S809, DAE21 and FX63100 airfoils. The grid refinement test and aerodynamic performances of rotors with high lift airfoils are studied.

2 Numerical Method

The preconditioned N-S equations in non-inertial general coordinates is given as

$$\Gamma \frac{\partial Q_p}{\partial t} + \frac{\partial E}{\partial \xi} + \frac{\partial F}{\partial \eta} + \frac{\partial G}{\partial \zeta} = \frac{\partial E_v}{\partial \xi} + \frac{\partial F_v}{\partial \eta} + \frac{\partial G_v}{\partial \zeta} + H \quad (1)$$

where t is time, (ξ, η, ζ) are general coordinates, $Q_p = [p, u, v, w, T, \tilde{v}]/J$ is the vector of primitive variables, (u, v, w) are velocity components in x, y and z directions, respectively, p is pressure, T is temperature, \tilde{v} is the turbulent variable in the Spalart-Allmaras (S-A) one-equation model. J is the Jacobian of coordinate transformation. The details of the preconditioning matrix Γ can be found in Ref. [9]. The convective flux and diffusive flux can be represented as (E, F, G) and (E_v, F_v, G_v) in the general coordinates. The source vector H is associated with parameters of the turbulence model as well as the non-inertial frame transformation [10].

The finite volume method is based on the local flux balance of each mesh cell. The semi-discrete form of Eq. (1) can be written as

$$\Gamma_{i,j,k} \left(\frac{Q_p^{n+1} - Q_p^n}{\Delta t} \right) = - \left[\tilde{E}_{i+1/2,j,k} - \tilde{E}_{i-1/2,j,k} \right] - \left[\tilde{F}_{i,j+1/2,k} - \tilde{F}_{i,j-1/2,k} \right] - \left[\tilde{G}_{i,j,k+1/2} - \tilde{G}_{i,j,k-1/2} \right] + H_{i,j,k}^{n+1} \quad (2)$$

where i, j, k is the control point of finite volume. A P-WENO numerical flux at a cell interface $i+1/2$ in direction i can be constructed as

$$\tilde{E}_{i+1/2,j,k} = \tilde{E}_{i+1/2,j,k}^{P-Roe} + \Gamma_{i+1/2} \tilde{E}_{i+1/2,j,k}^{H2} \quad (3)$$

where $\tilde{E}_{i+1/2,j,k}^{P-Roe}$ is the numerical flux of a first-order dissipative entropy satisfying scheme, in here, the preconditioned Roe scheme [9] is adopted, $\tilde{E}_{i+1/2,j,k}^{H2}$ is a high-order flux with WENO2 limiter. An implicit system was constructed through linearizing Eq. (2) about the preceding time, and the implicit equations were solved by the lower-upper symmetric Gauss-Seidel algorithm [11]. The detail formulation and numerical procedures for the P-WENO can be found in Ref. [1].

3 Configuration of NREL Phase VI Rotor

The NREL Phase VI rotor geometry, aerodynamic and structural properties are well-documented in the literatures [12][13]. The NREL Phase VI rotor consists of two blades. The blade is

designed using the NREL S809 airfoil profile, with a linear taper and a nonlinear twist. Wind speed is varied between 7 and 25m/s. The rotor is turning at a constant 72 rpm. The blade pitch is 3 degree towards feather relative to the rotor plane, there is no coning, and the blades are rigidly attached to the hub. The S configuration used the baseline blade with a length of 5.029m. Besides the S809 airfoil profile, rotors with high lift airfoils DAE21 and FX63100 are also studied to investigate their effects on aerodynamic performance of wind turbine rotors. The FX63 series was the first airfoil designed to operate at the low Reynolds numbers human power aircraft operate at Reynolds number approximately 1,000,000 and less. For FX63-100 airfoil, 1963 was the year it was designed in and 100 is 10 times the maximum thickness in percent. This airfoil has a large pitching moment and it also has a relatively thin trailing edge making construction difficult. In practice it is thickened with little effect on performance. The DAE 21 airfoil belongs to a family of airfoils designed for the Daedalus human power aircraft. The DAE 21 was used in the mid section of the wing, where the Reynolds number was intermediate (about 375,000). The maximum thickness is 11.9% locate at 32% chord. The profiles of S809, DAE-21, and FX63-100 airfoils are shown in Figure 1.

4 Computational Domain and Grid system

The structured grid system is commonly used in multidimensional problems since its memory requirement is less than that of the unstructured grid system for the same level of accuracy [14]. In our previous works, a solver with patched multi-block grid system was developed [1]. The patched multi-block grid system requires no matching connection, becomes a very good choice for saving the computer resource. The block interface condition is interpolated from the grid cells of the adjacent block. Although additional computer resource is spent on recording those relations and weightings for the interpolation, the overall computing cost is far below the wasted resource as in the matched grid system. Following the previous results, the present work adopts the patched multi-block grid system to discretize the spatial domain to further reduce the computational cost.

A parallel clustering algorithm based on Message Passing Interface (MPI) library was implemented. After the spatial domain is discretized by the patched multi-block grid system, all the blocks are allocated into different groups and then each group is assign to an individual processor for computing. In each processor, the interface conditions which are located in other processors are received from the corresponding processor through the MPI library. Similarly, the interface conditions which are necessary for the other processor are sent via MPI. Nevertheless, in problems with complex configuration, the deviation in cell number between different blocks may be huge. Simply assign the same number of blocks to each group can lead to unbalance loading for parallel computation. Further, the connection between blocks in the same group should be optimized to minimize the communication between processors. To balance the load among the computing nodes, Tabu search algorithm [15][16] is adopted to minimize this problem.

Due to cyclic conditions, only one of the two blades is modeled. The influence from the other blade is modeled by using periodic boundary condition at the cyclic plane of the computational domain. The computation domain extends to 4 and 12 blade lengths upstream and downstream, respectively, from the rotor plane. An C–O type inner grid with 369x45x231 grid points is considered as the benchmark fine grid system, which consists 369 points on blade surface in chordwise direction, 45 points in normal direction, and 231 point spanwise direction. The computational results of shaft torque are shown in Table 1. For the grids with 249 and 151 points in chordwise and spanwise directions, respectively, increasing grid points in normal direction up to 45 can reduce the relative error to 4.52%. If we fix 45 points in normal direction and vary the chordwise and spanwise points from 169 to 309 and from 101 to 191 respectively, the grid points increase from 739,200 to 1,636,800 points, the relative errors vary in the range from 5.32% to 0.46%.

Table 1, comparison the shaft torque in grid refinement test

Inner grid	Shaft torque(nt-m)	Relative error
169×45×101	986.42	5.32%
249×45×151	978.92	4.52%
309×45×191	932.23	0.46%
369×45×231	936.55	0(base)
249×29×151	2225.21	137%
249×37×151	1060.78	13.3%
249×65×151	956.86	2.17%

In our simulation, a patched multi-block grid system with 193 blocks and 249×65×151 inner grid system is adopted. The grid distribution on blade surface is shown in Figure 2. The y^+ values are kept below 2 on the blade surface. The total number of cells is about 3.06 million. It is noted that the cell number of matched multi-block grid system is over 6 million for the same block configuration around the blade. This clearly demonstrates the advantage of the patched grid system in computational efficiency.

5 Results and Discussion

5.1 Blade Surface Pressure Distributions

The influence of the tower is not taken into account. Due to cyclic conditions, only one of the two blades is considered. No-slip boundary condition is imposed on the blade surface. The influence of the other blade is included by using periodic boundary condition at the cyclic plane of the computational domain. At the upstream boundary, the incoming wind speed is specified. At the downstream boundary, a zero-gradient condition is imposed. Euler-slip conditions are applied at the lateral boundary located 3 blade lengths away from the blade tip. Since the non-inertial frame is adopted, the computational domain is rotating together with the blade under study. The 3-D numerical calculations of aerodynamic performance of the stall regulated NREL Phase VI Rotor under different inflow wind speeds ranging from 7 to 25 m/s are carried out. The rotating speed is fixed to 72 rpm. The final solution for each case is obtained with approximately 10000 iterations.

The pressure coefficient distributions at five primary spanwise locations: 30%, 46.6%, 63.3%, 80%, and 95% span are presented in Figure 3. It presents the computational results of wind speeds of 7, 10, 15, and 20m/s for rotors with all 3 airfoils and also the experimental data of rotor with S809 airfoil is plotted for comparisons. These experimental pressure distributions are very useful for the evaluation of numerical models accuracy in two ways: the occurrence of stall conditions on the blade can be easily identified and therefore the adequacy of the numerical model for stall prediction can be assessed, and also the accuracy/inaccuracy of the computed integrated loads (torque and bending moment) can be explained, however the modeling errors at various radial stations can actually compensate each other resulting in a good overall prediction of blade loads.

In general, our predictions and the measurements match well except for the regions around the leading edge of the blade with $r/R=0.3$ for wind speeds of 10 and 20 m/s and $r/R=0.47$ for wind speed of 10 m/s. These discrepancies may come from inaccurate prediction of flow separation. It should be noted that for airflow of wind turbine the results are very sensitive to the selection of turbulent model. Since the S-A one equation model is adopted in the present scheme, its limitation in predicting the location of flow separation is expected. For wind speeds less than 10m/s, the flow separation is weak and the S-A model is considered to perform well. The discrepancies may come from the transition between laminar and turbulent flows.

The 7 m/s case shows that the blade with S809 airfoil is not stalled, which is evident in the measured distributions. The computational results agree very well with the experimental data. For blades with DAE21 and FX63100 airfoils, the camber effects on pressure distribution provide more compression pressure on windward side and more suction pressure on leeward side than S809 airfoil does. The 10 m/s case shows that the blade with S809 airfoil is begin to stall at $r/R = 0.47$, which is evident in the measured distributions. The computational results agree very well with the experimental data except for the radial station of stall position that as many previous studies have not been able to reproduce the stall initiation. Noticeably the $r/R = 0.3$ section which is influenced by the inevitable flow separation and oblique vortex generated by the transition piece. For that matter, it seems that the geometrical approximation of this region of the blade does not have a discernible impact on the results. For blades with DAE21 and FX63100 airfoils, similar compression pressure on windward side as 7 m/s case obtained. But DAE21 airfoil provides more suction pressure than FX63100 airfoil on leeward side. At 15 m/s the blade is almost completely stalled except for the region near blade tip, which is evident in the measured distributions. For this case, the prediction of the pressure distribution is not so good; the pressure is under predicted on the first half of and over predicted on the latter half of the blade suction side at the sections of $r/R = 0.3$ and 0.8 . And the pressure is under predicted and over predicted of the blade suction side at the sections of $r/R = 0.63$ and 0.47 , respectively. This error does have a great impact on the overall forces. For blades with DAE21 and FX63100 airfoils, similar compression pressure on windward side as 7 m/s and 10 m/s cases obtained. But there is no significant difference of pressure distribution on leeward side among DAE21, FX63100 and S809 airfoil. At wing speed 25 m/s, the blade is completely stalled, however, the prediction of the pressure distribution agrees very well with the experimental data. Even though fully stalled, the surface pressure distributions are reasonably well computed.

5.2 Flow Field and Streamlines

Figure 4 shows the computational limiting streamline on blade suction surface of rotors with S809, DAE21 and FX63100 airfoils at wind speeds 7, 10, 15, and 20m/s. The flows upstream of the separation line are oriented parallel to the chord-wise direction, and the downstream flows are apparently in the radial direction. This implies that the airflow is fully 3-D for wind speeds > 7 m/s. For 7 m/s case, a separation line pattern for all three blades extends from near blade root to tip. For blade with S809 airfoil, the separation line locating at 60% chord near the root to 90% chord near the tip of blade is obtained for blade with S809 airfoils. For blade with DAE21 airfoil, the separation line locating is similar to the S809 case in root and intermediary sections, but moves forward in tip. For FX63100 airfoil, the separation line retreats to 80% chord in intermediary sections, and to trailing edge in near tip sections. When the wind speed increases to 10m/s, the separation line moves forward and the radial flows are increased, especially for blade with FX63100 airfoil. Just along the line of separation there appears to be a focus of separation on the surface. This translates into the small region of the flow curling under itself forming a secondary vortex. The formation of this secondary vortex usually is accompanied by separation. Several focuses of separation appeared along spanwise direction near the outboard of blade. The streamlines become more complicated with the increasing of wind speed. For wind speed of 15m/s, the flows separate at the leading edge of the blade, and a re-attached line near the trailing edge of the blade are found. The focuses of separation still on blades of S809 and DAE21 airfoil, but disappeared on FX63100 airfoil. For wind speed of 25m/s, the flows separate at the leading edge of the blade, from root to tip, eventually leading to a fully detached flow for all three types of blade. At wind speeds 15 and 25 m/s, the surface streamlines indicate that the boundary layer flow is not only in spanwise direction, from root to tip, but also in streamwise direction, from blade trailing to leading edge.

5.3 Aerodynamic Torque and Thrust

Figure 5 presents a comparison between the experimentally measured values of turbine torque with S809 airfoil and the numerically computed values of turbine torque with S809, DAE21 and FX63100 airfoils. For S809 airfoil, the computed shaft torque is roughly close to and with similar trend as the measurement results. The predicted shaft torques are larger than the experimental data for inlet wind speeds of 10, 13, 15m/s. The differences between our calculations and the experiment are approximately less than 10 %. As mentioned before, these discrepancies may come from inaccurate prediction of flow separation. Moreover, some uncertainties in experiment setup and measurement could also contribute to these mismatches. The rotor with DAE21 airfoil can achieve the highest shaft torque in the range of wind speed less than 20m/s. The DAE21 airfoil increased the shaft torque up to 40% in the region of the wind velocity near 15m/sec where the blades stall growing. For higher wind speed, the effects of airfoil on rotor shaft torque are not significant. In contrast, the FX63100 airfoil got the lowest shaft torque in the full range of wind speed investigated in the present work. It is not surprising since the lift coefficient of FX63100 airfoil is significantly lower than the other two.

For the root flap moment, Figure 6 presents a comparison between the experimentally measured values with S809 airfoil and the numerically computed values with S809, DAE21 and FX63100 airfoils. For S809 airfoil, the computed the root flap moment agrees well with experimental data for wind speeds less than 15m/s. The predicted root flap moments are lower than the experimental data for wind speeds great than 15m/s where the blades stalled. Our calculations are approximately under predicted about 15 %. A clear interpretation of these results cannot yet be given based on the available information. Probably after testing several turbulence models or even modifying the solver setup, or improving the mesh, a tendency may appear, or other type of evidence which might help in the assessment of the numerical model performance. Nevertheless, it is evident that the current model is capable of predicting the stall initiation for this particular geometrical configuration, which is a very desirable quality taking into account the fact that NREL Phase VI rotor is a stall-regulated wind turbine. One of the parameters which could have an important impact on the solution is the accuracy of the transition location prediction on the blade. Both the rotors with DAE21 and FX63100 airfoil produced higher root flap moment in the full range of wind speed investigated in the present work. This characteristic is not conducive to designing the blade structures.

6 Conclusions

This paper presented a comparison of the performance predictions of the NREL Phase VI rotor with S809, DAE21 and FX63100 airfoils by using P-WENO high order scheme to solve preconditioned Navier-Stokes equations with Spalart-Allmaras single-equation turbulence model, and Eppler, Chen-Thyson transition position computing model in non-inertial frame. The results show that using a relatively fine mesh, the numerical model is able to give a reasonable evaluation of turbine torque and blade root flap bending moment in the range of wind velocity from 7 m/s to 25 m/s, including pre-stall and post-stall regimes. The DAE21 airfoil increased the shaft torque up to 40% in the region of the wind velocity near 15m/sec where the blades stall growing. For higher wind speed, the effects of airfoil on rotor shaft torque are not significant. In contrast, the FX63100 airfoil got the lowest shaft torque in the full range of wind speed investigated in the present work. Both the rotors with DAE21 and FX63100 airfoil produced higher root flap moment in the full range of wind speed. This characteristic is not conducive to designing the blade structures. The present work will be extended in the future with further investigations of the optimization of blade aerodynamic design of wind turbine rotor.

Acknowledgement: JYY thanks the support from National Science Council, Taiwan through Grants NSC 99-2221-E002-084-MY3 and 100-2221-E002-106-MY3. And, J. C. Huang thanks the support from National Science Council, Taiwan through Grants NSC 100-2221-E-019-048-MY3.

References

- [1] J.-C. Huang, H. Lin and J.-Y. Yang, "Implicit Preconditioned WENO Scheme for Steady Viscous Flow Computation," *Journal of Computational Physics*, Vol. 228, Issue 2, Feb. 2009, 420-438.
- [2] J.-C. Huang, H. Lin, T.-J. Hsieh, T.-Y. Hsieh, "Parallel Preconditioned WENO Scheme for Three-dimensional Flow Simulation of NREL Phase VI Rotor," *Computers and Fluids*, Vol. 45, Issue 1, June 2011, pp. 276-282.
- [3] J. Y. Yang, T. J. Hsieh, and C. H. Wang, "Implicit WENO schemes with anti-diffusive flux for the compressible viscous flow computations," *AIAA J.*, Vol. 47, 2009, pp. 1435-1444.
- [4] M. S. Selig and J. J. Guglielmo, "High-Lift Low Reynolds Number Airfoil Design," *J. of Aircraft*, Vol. 34, No. 1, Jan.-Feb. 1997, pp. 72-79.
- [5] W. P. Wolfe and S. S. Ochs, "CFD Calculations of S809 Aerodynamic Characteristic," *AIAA Paper NO. 97-0973*
- [6] G. Xu and L. N. Sankar, "Effects of Transition, Turbulence and Yaw on the Performance of Horizontal Axis Wind Turbines," *AIAA-2000-0048*, 2000.
- [7] S. Benjanirat and L. N. Sankar, "Evaluation of Turbulence Models for the Prediction of Wind Turbine Aerodynamics," *AIAA-2003-0517*, 2003
- [8] R. Eppler, "Airfoil Design and Data," New York, NY, Springer-Verlag, 1990.
- [9] J. M. Weiss and W. A. Smith, "Preconditioning Applied to Variable and Constant Density Flows," *AIAA Journal*, 33:2050-2057, 1995.
- [10] L. B. Schiff and J. L. Steger, *Numerical Simulation of Steady Supersonic Viscous Flow*. *AIAA Journal*, 18:1421-1430, 1980.
- [11] S. Yoon and D. Kwak, *Implicit Navier–Stokes Solver for Three-dimensional Compressible Flows*. *AIAA Journal*, 30:2653-2659, 1992.
- [12] M. M. Hand, D. A. Simms, L. J. Fingersh, D. W. Jager, J. R. Cotrell, S. Schreck and S. M. Larwood, *Unsteady Aerodynamics Experiment Phase VI: Wind Tunnel Test Configurations and Available Data Campaigns*. NREL/TP-500e29955; 2001.
- [13] D. A. Simms, S. Schreck, M. Hand and L. J. Fingersh, "NREL Unsteady Aerodynamics Experiment in the NASA-Ames Wind Tunnel: A Comparison of Predictions to Measurements," NREL/TP-500-29494, June 2001.
- [14] C. Hirsch, *Numerical Computation of Internal and External Flows*. John Wiley & Sons Inc, 1988.
- [15] F. Glover, *Tabu search-Part I*. *ORSA Journal on Computing*, Vol. 1, No. 3, Summer, 1989.
- [16] F. Glover, *Tabu search-Part II*. *ORSA Journal on Computing*, Vol. 2, No. 1, Winter, 1990.

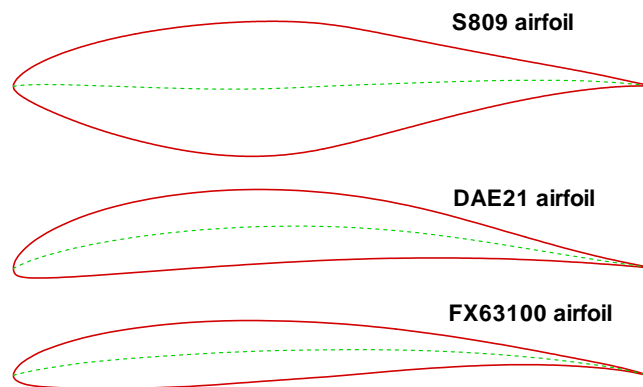


Figure 1, Comparison the profiles of S809, DAE21 and FX63100 airfoils

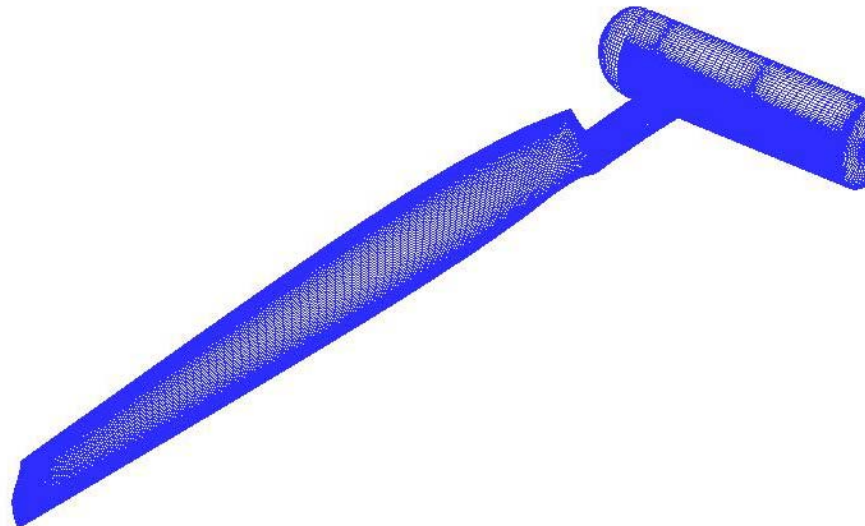
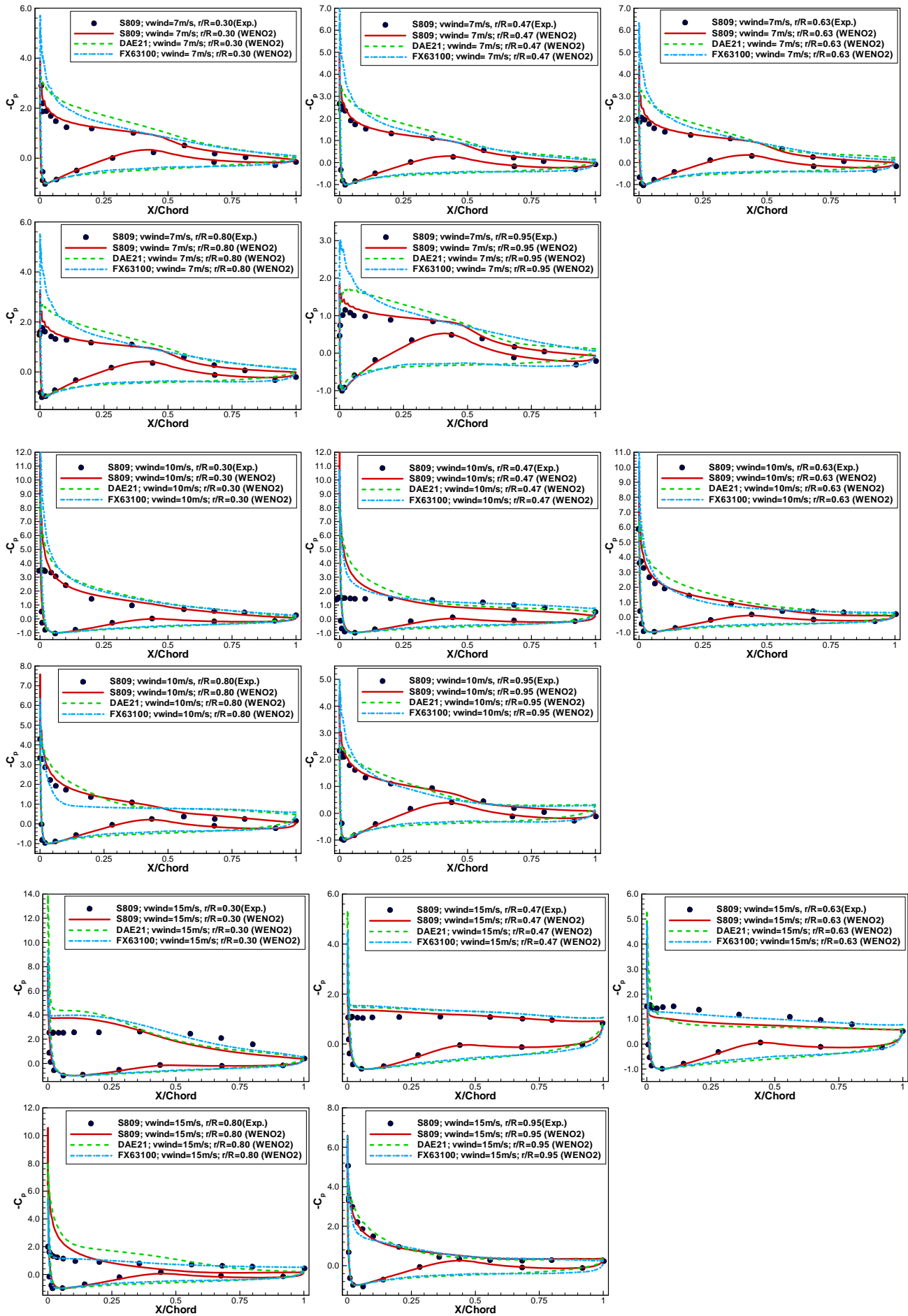


Figure 2, Grid distributions on blade surface



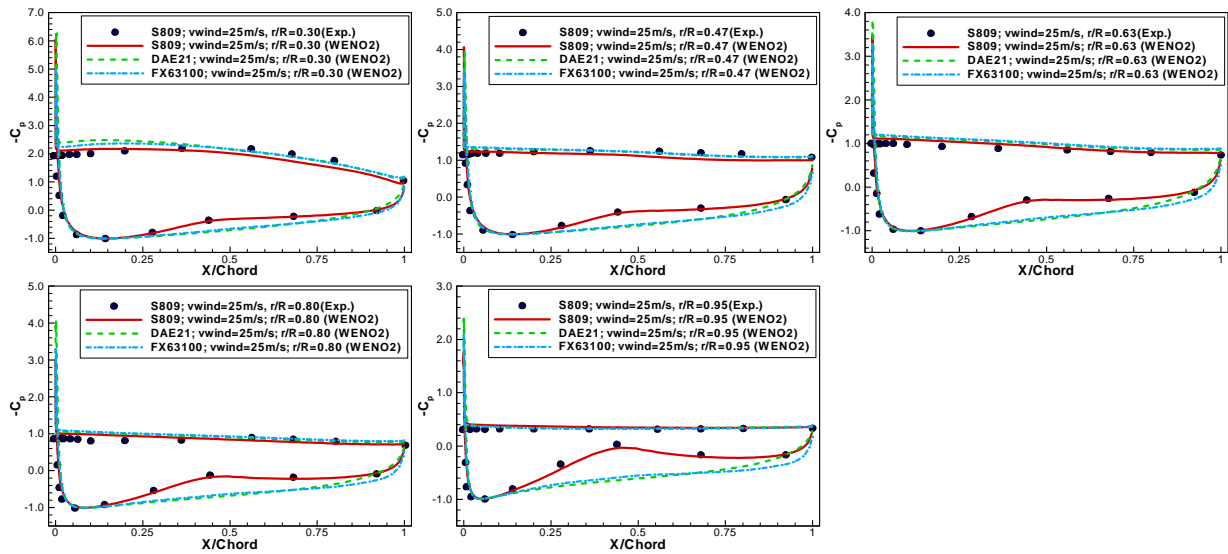


Figure 3, Comparison of the pressure coefficients among the blades with S809, DAE21 and FX63100 airfoils at five spanwise locations: 30%, 46.6%, 63.3%, 80%, and 95% span.

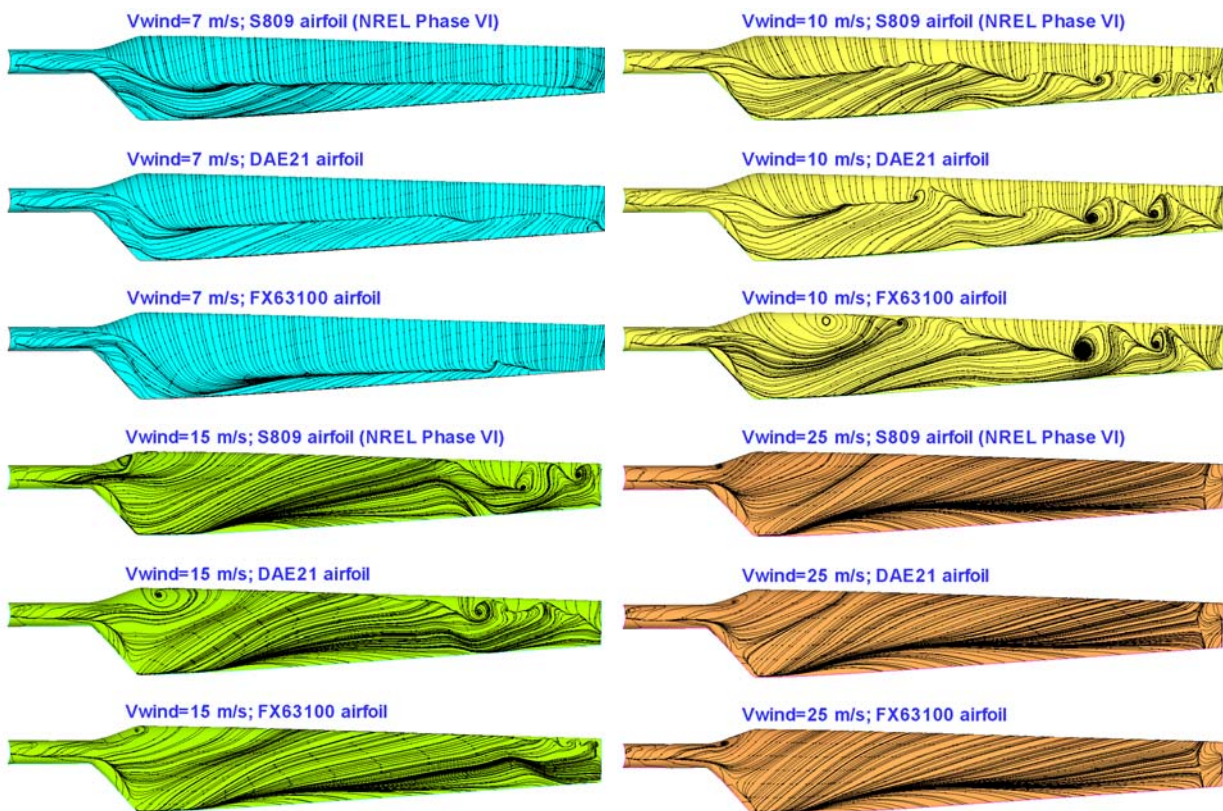


Figure 4, The computational limiting streamline on blade suction surface of rotors with S809, DAE21 and FX63100 airfoils at wind speeds 7, 10, 15, and 20m/s.

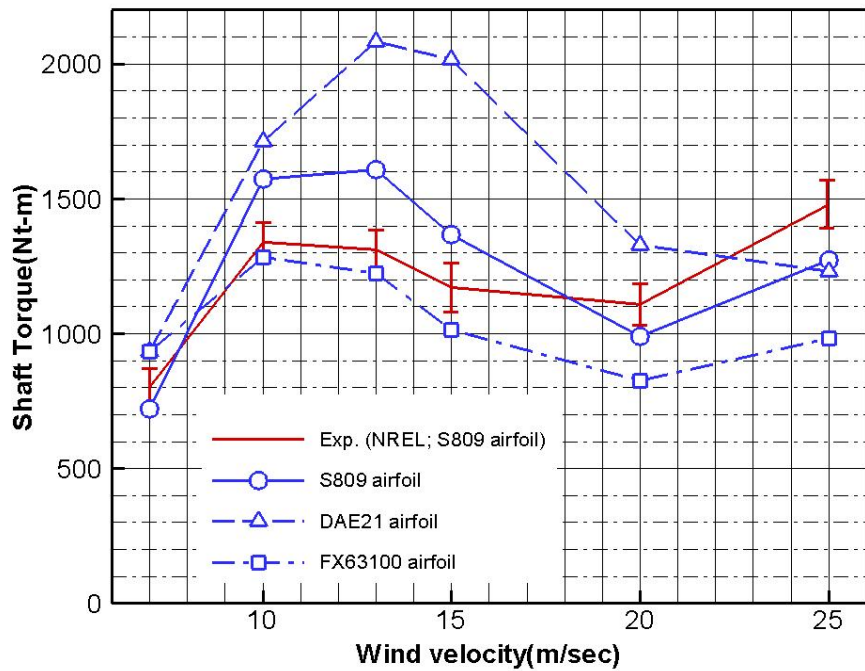


Figure 5, Comparison of shaft torque among rotors with different airfoils.

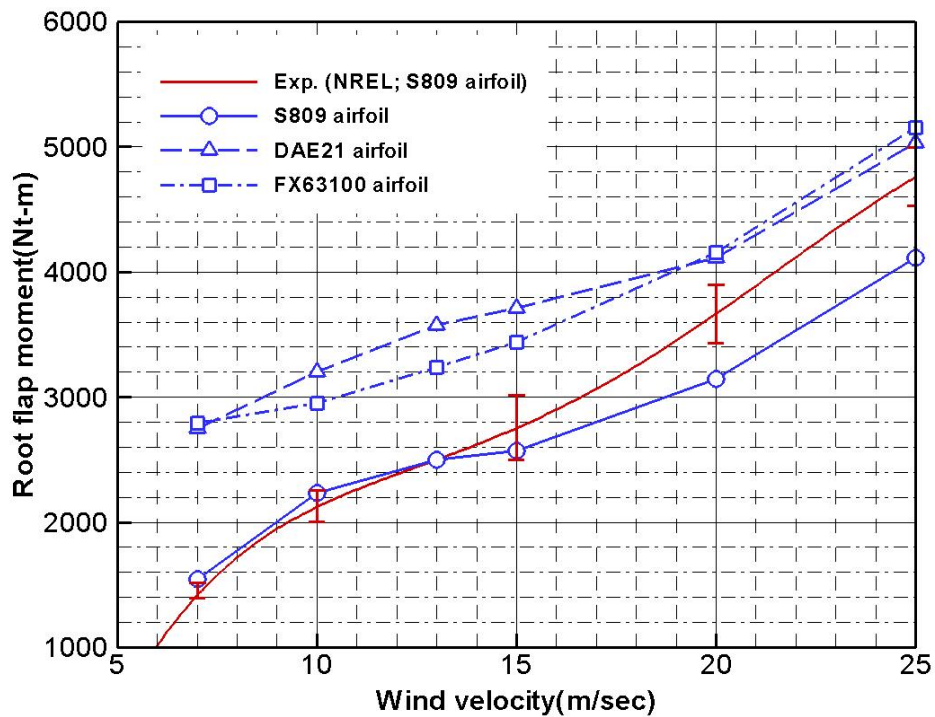


Figure 6, Comparison of root flap moments among the experimental values of blades with S809 airfoil and the numerically computed values with S809, DAE21 and FX63100 airfoils